

## Alignment of Hurricane-like Vortices on $f$ and $\beta$ Planes

ROBERT W. JONES AND HUGH E. WILLOUGHBY

*Florida International University, Miami, Florida*

MICHAEL T. MONTGOMERY

*Naval Postgraduate School, Monterey, California*

(Manuscript received 5 June 2008, in final form 17 November 2008)

### ABSTRACT

A nonlinear, two-layer, vortex-tracking semispectral model (i.e., Fourier transformed in azimuth only) is used to study the evolution of dry, but otherwise hurricane-like, initially tilted vortices in quiescent surroundings on  $f$  and  $\beta$  planes. The tilt projects onto vorticity asymmetries that are dynamically vortex Rossby waves.

Since the swirling wind in the principal mean vortex used here decays exponentially outside the eyewall, it has an initial potential vorticity (PV) minimum. The resulting reversal of PV gradient meets the necessary condition for inflectional (i.e., barotropic or baroclinic) instability. Thus, the vortex may be inflectionally stable or unstable. On an  $f$  plane, the tilt precesses relatively slowly because the critical radius, where the phase speeds of the waves match the mean swirling flow, is far from the center. An alternative Gaussian-like PV monopole that has a monotonic outward decrease of PV is stable to inflectional instability. It has a smaller critical radius and rapid tilt precession. Generally, vortices with fast tilt precession are more stable, as are stronger vortices in higher latitudes.

On a  $\beta$  plane, the interaction between the symmetric vortex and the planetary PV gradient induces  $\beta$  gyres that push the vortex poleward and westward. The interaction between the  $\beta$  gyres and the planetary PV gradient may either create a PV minimum or intensify a minimum inherited from the initial condition. Thus, the nonlinear  $\beta$  effect reduces the ability of the vortex to recover from initial tilt, relative to the same vortex on an  $f$  plane. This result contrasts with previous studies of barotropic vortices on  $f$  planes, where the linear and nonlinear solutions were nearly identical.

### 1. Introduction

Tropical cyclone (TC) response to environmental vertical shear is crucial to forecasting motion and intensity. It involves both latent heat release that maintains or intensifies the vortex and adiabatic vortex adjustment or wave processes. While latent heating is essential in nature and has been shown (Schechter and Montgomery 2007) to suppress unstable gravity wave radiation from tilted vortices, we focus here on dry mechanisms. The model used is an elaboration of the vortex tracking semispectral (VTSS) models of Willoughby (1992, 1994, 1995) and Willoughby and Jones (2001). We extend the shallow-water barotropic dynamics to two active layers,

still with no heating or vertical mixing, and run both linear and nonlinear variants on  $f$  and  $\beta$  planes.

TC-like vortices may recover from imposed tilt or resist environmental wind shear in ways that do not involve vertical coupling through latent heating. Jones (1995) showed that vortex tilt projects onto vortex Rossby waves (VRWs) that precess around the vortex toward the left side of the shear vector. VRWs are asymmetric vorticity waves that propagate on the radial gradient of axially symmetric mean relative vorticity (Montgomery and Kallenbach 1997; Möller and Montgomery 1999). When the mean relative vorticity decreases outward, VRWs propagate upstream with phase velocity generally slower than either the mean flow or the phase propagation of inertia-gravity waves. In the Jones study, the upper vortex tended to realign after 180 degrees of precession, when the shear forced it back toward the lower vortex, provided that the shear was not strong enough to blow off the vortex top. Jones noted

---

Corresponding author address: H. E. Willoughby, Department of Earth Sciences, Florida International University, University Park Campus, PC 344, Miami, FL 33199.  
E-mail: hugh.willoughby@fiu.edu

Report Documentation Page				Form Approved OMB No. 0704-0188	
Public reporting burden for the collection of information is estimated to average 1 hour per response, including the time for reviewing instructions, searching existing data sources, gathering and maintaining the data needed, and completing and reviewing the collection of information. Send comments regarding this burden estimate or any other aspect of this collection of information, including suggestions for reducing this burden, to Washington Headquarters Services, Directorate for Information Operations and Reports, 1215 Jefferson Davis Highway, Suite 1204, Arlington VA 22202-4302. Respondents should be aware that notwithstanding any other provision of law, no person shall be subject to a penalty for failing to comply with a collection of information if it does not display a currently valid OMB control number.					
1. REPORT DATE <b>NOV 2008</b>		2. REPORT TYPE		3. DATES COVERED <b>00-00-2008 to 00-00-2008</b>	
4. TITLE AND SUBTITLE <b>Alignment of Hurricane-like Vortices on f and b Planes</b>				5a. CONTRACT NUMBER	
				5b. GRANT NUMBER	
				5c. PROGRAM ELEMENT NUMBER	
6. AUTHOR(S)				5d. PROJECT NUMBER	
				5e. TASK NUMBER	
				5f. WORK UNIT NUMBER	
7. PERFORMING ORGANIZATION NAME(S) AND ADDRESS(ES) <b>Naval Postgraduate School, Department of Meteorology, Monterey, CA, 93943</b>				8. PERFORMING ORGANIZATION REPORT NUMBER	
9. SPONSORING/MONITORING AGENCY NAME(S) AND ADDRESS(ES)				10. SPONSOR/MONITOR'S ACRONYM(S)	
				11. SPONSOR/MONITOR'S REPORT NUMBER(S)	
12. DISTRIBUTION/AVAILABILITY STATEMENT <b>Approved for public release; distribution unlimited</b>					
13. SUPPLEMENTARY NOTES					
14. ABSTRACT <b>A nonlinear, two-layer, vortex-tracking semispectral model (i.e., Fourier transformed in azimuth only) is used to study the evolution of dry, but otherwise hurricane-like, initially tilted vortices in quiescent surroundings on f and b planes. The tilt projects onto vorticity asymmetries that are dynamically vortex Rossby waves. Since the swirling wind in the principal mean vortex used here decays exponentially outside the eyewall, it has an initial potential vorticity (PV) minimum. The resulting reversal of PV gradient meets the necessary condition for inflectional (i.e., barotropic or baroclinic) instability. Thus, the vortex may be inflectionally stable or unstable. On an f plane, the tilt precesses relatively slowly because the critical radius, where the phase speeds of the waves match the mean swirling flow, is far from the center. An alternative Gaussian-like PV monopole that has a monotonic outward decrease of PV is stable to inflectional instability. It has a smaller critical radius and rapid tilt precession. Generally, vortices with fast tilt precession are more stable, as are stronger vortices in higher latitudes. On a b plane, the interaction between the symmetric vortex and the planetary PV gradient induces b gyres that push the vortex poleward and westward. The interaction between the b gyres and the planetary PV gradient may either create a PV minimum or intensify a minimum inherited from the initial condition. Thus the nonlinear b effect reduces the ability of the vortex to recover from initial tilt, relative to the same vortex on an f plane. This result contrasts with previous studies of barotropic vortices on f planes, where the linear and nonlinear solutions were nearly identical.</b>					
15. SUBJECT TERMS					
16. SECURITY CLASSIFICATION OF:			17. LIMITATION OF ABSTRACT <b>Same as Report (SAR)</b>	18. NUMBER OF PAGES <b>14</b>	19a. NAME OF RESPONSIBLE PERSON
a. REPORT <b>unclassified</b>	b. ABSTRACT <b>unclassified</b>	c. THIS PAGE <b>unclassified</b>			



that the tilted gyres remained nearly in gradient balance about their displaced centers during this interaction.

This description has a good deal in common with propagation and life cycles of convective cells observed with airborne radar in Hurricanes Jimena and Olivia (Black et al. 2002). In convection-resolving numerical simulations (e.g., Frank and Ritchie 1999, 2001), dry processes localize eyewall ascent on the downshear side of the eye, or even to the right of downshear. As moist ascent becomes dominant, the simulated convection advects around the eye to the left side of the shear vector, as observed. Even though diabatic processes in the vortex cores of real hurricanes evolve on much faster time scales than the dry mechanisms analyzed here, evolution of the outer vortex and its interaction with VRW asymmetries take place 200–400 km from the vortex center. In nature, this region corresponds to a moat of diabatically induced descent and generally suppressed latent heat release.

Reasor et al. (2004) demonstrated two alternative dry mechanisms for vortex realignment. They noted that the asymmetry due to the tilt projected onto radially sheared VRWs and a “quasi mode.” Outside the radius of maximum wind  $R_{\max}$ , the sheared VRWs were differentially advected by the radially shearing mean flow. They took the form of spirals in the potential vorticity (PV) field. PV filamentation quickly reduced the tilt amplitude as the VRWs propagated outward. This was the “spiral windup” mechanism for reducing vortex tilt. In addition, most vortices also supported a quasi mode, a superposition of adjacent VRW eigenmodes. The quasi mode’s components resonated between the center or an inner Rossby wave turning point and an outer critical radius where the frequency of the cyclonically precessing VRWs matched the orbital period of the mean flow. Higher resonant orbital periods correlated with smaller critical radii. When the outer mean PV gradient had the same sign as in the inner core, the intrinsic wave propagation was the same in both regions, and the quasi mode decayed by resonant absorption of wave activity at the critical radius. The difference between the sheared VRWs and the quasi mode is that the former is a freely propagating wave that always loses energy (i.e., the sum of the kinetic and available potential energies of the asymmetric projection of the tilted symmetric vortex) through PV filamentation, whereas the latter is a superposition of radially trapped waves (eigenmodes) that may either lose energy through absorption at the critical radius or gain energy by overreflection at the critical radius. This phenomenon, sometimes termed “critical layer mixing” or “PV stirring,” is a second dry mechanism that can make vortices resistant to environmental shear.

When an outer PV minimum is present, the PV gradient at the critical radius may be opposite in sign from that in the inner core and resonant amplification will occur. The amplifying gyre is a discreet VRW eigenmode. Amplification may also occur when the critical radius is located on the stable side of the PV minimum. These instabilities result from advection of PV across the PV minimum by tilt VRWs that are phase-locked in time, but have a significant phase shift across the PV minimum, so that advective PV transports across the PV minimum amplify the VRWs. This is the type-2 instability (inflectional) of Kossin et al. (2000), but generalized to wave-number 1. It is also an example of barotropic instability.

The principal vortex used here has solid rotation inside  $R_{\max}$  and exponential decay of the wind outside  $R_{\max}$ . A PV minimum, which may be stable or unstable, is always present. Tilts of PV monopole vortices, such as the Gaussian profile used by Reasor et al. (2004), precess faster than those of exponential-decay vortices because the shorter orbital periods of the swirling wind at smaller critical radii lead to higher resonant orbital frequencies. They are initially stable to inflectional (i.e., generalized barotropic or baroclinic) instability. Either vortex may eventually evolve to an unstable shape through nonlinear processes.

A key result here is that the “ $\beta$  torque,” which arises from conservation of PV as the vortex moves poleward toward larger values of  $f$ , either creates a PV minimum or strengthens a preexisting PV minimum. Thus, an initially stable vortex can become unstable to inflectional instability or at least become less stable and arguably less resilient to environmental shear.

If the tilt precession frequency exceeds the local inertia frequency, inertia-gravity waves may resonate unstably with the tilt VRW at the critical radius. We postpone analysis of this instability to a future study. Here we avoid it through use of sufficiently stable PV gradients at the critical radius (Schechter and Montgomery 2004) and comparatively small initial tilts. This strategy avoids reduction of the mean PV gradient below the value required to suppress inertia-gravity wave radiation (Schechter and Montgomery 2006).

These instabilities have not yet been observed in real TCs. Detection would be challenging in the present state of hurricane observations, but airborne Doppler radar is an increasingly promising tool. Model details appear in section 2, followed by inflectional instability results in section 3. Section 4 is the summary.

## 2. Vortex tracking model

We analyze the stability of tilts imposed through the initial condition on  $f$  and  $\beta$  planes with the ultimate goal

of understanding vortex responses to environmental shear. The key to both the tilted and sheared problems lies in the internal dynamics that act to restore vertical alignment and should be much the same in either case. Analysis of initially imposed tilt avoids the complexity that arises from environmental PV gradients and vertically changing environmental relative motions.

The basic model is an elaboration of the VTSS model of Willoughby (1994). It is a dry, nonlinear, shallow-water model set in cylindrical coordinates that move with the vortex center. The flow is partitioned into vortex and environment. The environmental flow (set to zero here) does not evolve with time. The axially symmetric part of the swirling wind is in gradient balance with the mass field and has a secondary circulation described by a Sawyer–Eliassen equation. Vortex asymmetries are represented spectrally in azimuth and with finite differences in radius and time.

The original single-layer model is extended to two homogeneous, incompressible layers topped by either a free surface or an inertialess upper layer. Layer 1 is the lowest, in contact with the surface; layer 2 is in the middle; layer 3 is the top, inertialess layer (Fig. 1). When used, the inertialess layer is essential to construction of initially barotropic vortices and to scaling the equivalent depth to a realistic value. The governing equations are the same as in Willoughby and Jones (2001):

$$\begin{aligned} \frac{\partial \mathbf{v}_k}{\partial t} + (\zeta_k + f)\mathbf{k} \times \mathbf{v}_k + \nabla \left[ \frac{1}{2}(\mathbf{v}_k \cdot \mathbf{v}_k) + \frac{p_k}{\rho_k} \right] \\ = (\mathbf{c} - \tilde{\mathbf{c}}_k) \cdot \nabla \mathbf{v}_k - \mathbf{v}_k \cdot \nabla \tilde{\mathbf{c}}_k + \mathbf{F}_{vk}, \\ \frac{\partial h_k}{\partial t} + \nabla \cdot (h \mathbf{v}_k) = (\mathbf{c} - \tilde{\mathbf{c}}_k) \cdot \nabla h_k - \mathbf{v}_k \cdot \nabla \tilde{h}_k + F_{hk}. \end{aligned} \quad (1)$$

Here  $\mathbf{v}_k$ ,  $\zeta_k$ ,  $h_k$ ,  $p_k$ , and  $\rho_k$  are the velocity, relative vorticity, thickness, pressure, and density in the  $k$ th layer;  $\mathbf{k}$  is the vertical unit vector (not to be confused with the layer index);  $f = f_0 + \beta y$  is the Coriolis parameter, where  $y$  is the meridional coordinate in the moving reference frame;  $\mathbf{c}$  is the vortex motion;  $\tilde{\mathbf{c}}_k$  is the geostrophic environmental flow;  $\tilde{h}_k$  is the environmental perturbation layer thickness; and  $\mathbf{F}_{vk}$  and  $F_{hk}$  represent horizontal mixing. Nonlinear terms are computed as in Willoughby and Jones (2001).

The layers interact through hydrostatic pressure forces and a small coupling through the radial mean-wind equation. There is no bottom topography and no vertical mixing or surface drag. Horizontal mixing is present with a sponge region filling the outer 500 km of the domain. The pressure gradient accelerations in the lower (1) and upper (2) layers are

$$\frac{1}{\rho_1} \nabla p_1 = g \sigma_{13} \nabla (h_1 + h_2) + g \sigma_{12} \nabla h_1 \quad (2)$$

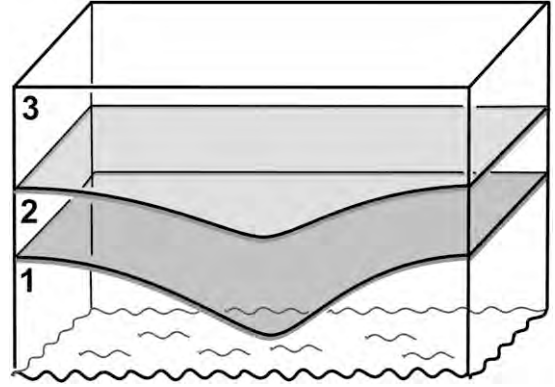


FIG. 1. The arrangement of layers in the model: Layer 3 is the inert upper layer with fluid density  $\rho_3$ . Layers 2 and 1 are the active layers with densities  $\rho_2$  and  $\rho_1$ .

and

$$\frac{1}{\rho_2} \nabla p_2 = g \sigma_{23} \nabla (h_1 + h_2), \quad (3)$$

where  $g$  is gravity;  $\sigma_{13} = (\rho_2 - \rho_3)/\rho_1$ ,  $\sigma_{12} = (\rho_1 - \rho_2)/\rho_1$ , and  $\sigma_{23} = (\rho_2 - \rho_3)/\rho_2$  are density ratios between the layers. When the fluid has a free surface,  $\rho_3 = 0$ . This case, which is standard, uses  $\rho_1 = 10$  and  $\rho_2 = 9.5$ , producing static stability  $\sigma_{12} = 0.05$ . With default layer depths of 4000 m, the external gravity wave speed is  $278 \text{ m s}^{-1}$  and the internal wave speed is  $32 \text{ m s}^{-1}$ . For these parameters, the internal Rossby radius of deformation based upon planetary rotation alone is  $L_2 = \sqrt{g \sigma_{12} h_2 / 2 f^2} = 900 \text{ km}$  at  $20^\circ$  latitude (Ooyama 1969).

The model is integrated on a 4000-km circular domain with a 4-km radial mesh. We generally use wavenumber-3 spectral truncation. Most results have been verified with wavenumber-6 truncation, although some strong vortices required a 2-km mesh to avoid inertia-gravity wave instability with wavenumber-8 truncation. We also use a linear model, in which the base vortex is held fixed with only a wavenumber-1 asymmetry.

The horizontal mixing coefficient is  $10 \text{ m}^2 \text{ s}^{-1}$  for the symmetric vortex and  $1000 \text{ m}^2 \text{ s}^{-1}$  for the asymmetric components. The former value was chosen to prevent excessive decay of the vortex; the later was chosen to control computational noise. Additional mixing, 10 times normal for the symmetric component and 20 times for the asymmetric, is imposed near the center to control noise from the center boundary condition and potential instabilities inside the eye. Experiments with larger mixing coefficients produced sensibly the same results.

The vortex tracking scheme follows the center of the lower vortex. At each time step the center coordinates are extrapolated linearly forward using the vortex

velocity from the immediate past step. Vortex position is corrected at each time step (usually 15 s) by  $\alpha$ -gyre closure, which relocates the center to remove the apparent asymmetry. The  $\alpha$  gyres (Willoughby 1992), or pseudomode (Montgomery et al. 1999), are an apparent wavenumber-1 streamfunction asymmetry that arises from mislocation of the axially symmetric vortex center. Mathematically it is the negative vector triple product of the center displacement vector, the vertical unit vector, and the axially symmetric mean wind. In these calculations, typical acceleration corrections are a few meters at the beginning of experiments but decrease to a few centimeters later. Although these values seem small, they reflect the precision of the tracking algorithm and are essential to avoiding wavenumber  $\geq 2$  corrections in the  $\alpha$  gyres. The same correction is applied to both levels so that a residual pseudomode remains in the upper layer. It is used to track the position of the upper vortex relative to the lower.

The static stability is chosen to match the  $8 \text{ m s}^{-1}$  westerly shear (zero mean) case of Reasor et al. (2004) at  $12.3^\circ$  north using their Gaussian vortex with  $40 \text{ m s}^{-1}$  maximum wind at 100-km radius. Their model had ten 1-km layers with a rigid lid. It was continuously stratified and compressible with constant static stability. The first forced cyclonically precessing loop had  $\sim 60$ -km amplitude (their Fig. 9), and the vortex remained coherent with a precessing tilt (their Fig. 8). When their vortex was inserted into the VTSS model, the corresponding loop amplitudes were 72 km. Perfect matching of loop amplitude is not possible because our initial vortex is slightly baroclinic and our default depth is smaller, implying more stable loops. Truncation here is at wavenumber 3 or 6, whereas Reasor et al. used 8. Static stability cannot be lowered below  $\sigma_{12} = 0.01$  in the VTSS model because the resulting small Rossby radius leads to inertial oscillations that spread to the boundary.

The wavenumber- $n$  PV in model layer  $k$  is as given by Willoughby (1994):

$$\text{PV}_{nk} = \frac{\zeta_{nk} + \beta y \delta_{n,1}}{H_k} - \frac{(\zeta_{0k} + f)h_{nk}}{H_k^2}. \quad (4)$$

Here  $\zeta_{nk}$  is the asymmetric relative vorticity,  $\zeta_{0k}$  is the axially symmetric vorticity,  $h_{nk}$  is the asymmetric layer depth,  $H_k$  is the sum of the resting depth and the depth perturbation in gradient balance with the axially symmetric wind  $v_{0k}$ ,  $\beta$  is the planetary vorticity gradient, and  $\delta_{n,1}$  is the Kronecker delta function, equal to 1 when  $n = 1$  and zero otherwise. The axially symmetric PV is  $\text{PV}_{0k} = (\zeta_{0k} + f)/H_k$ .

Barotropic initial vortex structures are possible only when the layer depths are equal and densities have ra-

tios of 3:2:1 for the lower, upper, and inert layers. We call this state “passive” stratification because initially aligned barotropic vortices do not separate in the absence of environmental shear. This is the only stratification that has the same PV in both active layers, a configuration that is not possible with our default stratification.

All initial vortices have cyclonic winds throughout. The standard vortex used here (Fig. 2a) has solid rotation inside  $R_{\max}$  and exponential decay outside  $R_{\max}$  (Willoughby et al. 2006). It has maximum winds  $40 \text{ m s}^{-1}$  at 40-km radius. The exponential decay length  $X_1$  is based on analysis of research aircraft observations (Mallen et al. 2005). Larger values of  $X_1$  imply a broader vortex in which the wind decreases more gradually with radius,  $r > R_{\max}$ . By fitting the exponential vortex to mean data between  $R_{\max}$  and  $3R_{\max}$  for pre-hurricanes, minimal hurricanes, and strong hurricanes, we choose decay factors  $X_1 = 240, 208$ , and  $160 \text{ km}$ , respectively. Even though the winds are the same in each layer, the mass gyres are not because of the non-passive stratification.

The new vortex has a monotonic radial decrease of angular velocity so that it is free from the Nolan and Montgomery (2000) instability, unlike similar vortices in Willoughby (1995) and Willoughby and Jones (2001). Although there is a broad, outer PV minimum that meets the *necessary* condition for barotropic instability, the initial vortex is barotropically stable as well (Fig. 2b). In the presence of vertical shear or with very low horizontal mixing, the vortex profile could evolve to an unstable configuration. We eliminate the discontinuity in the mean-flow vorticity gradient between solid rotation and exponential decay at  $R_{\max}$  by increasing the solid rotation around the center by 10%, setting the wind at  $R_{\max}$  to its specified value, and smoothing (Fig. 2a). Experiments with and without this correction yield essentially the same results.

The Rossby number at  $r = R_{\max}$  is  $\text{Ro} = V_{\max}/f R_{\max}$ , where  $V_{\max}$  is the maximum wind. For the standard vortex,  $\text{Ro} = 20$  and the ratio of  $R_{\max}/L_2 = 0.04$ . This initial state was a little above the curve in Fig. 3 of Reasor et al. (2004), but the standard vortex should be dominated by the quasi mode, as described below. Note that Reasor et al. based their diagram on a Gaussian vortex that had significantly different structure from our standard vortex.

Here we analyze two other vortices (Fig. 2a). A Gaussian vortex was used only to tune the model stability. With  $R_{\max}$  reduced from 100 to 40 km, the tilted or sheared Gaussian vortex radiated unstable inertia-gravity waves. These waves resonate at a VRW critical radius where the vortex PV gradient was too weak to suppress the instability. Instead, we used the smoothed



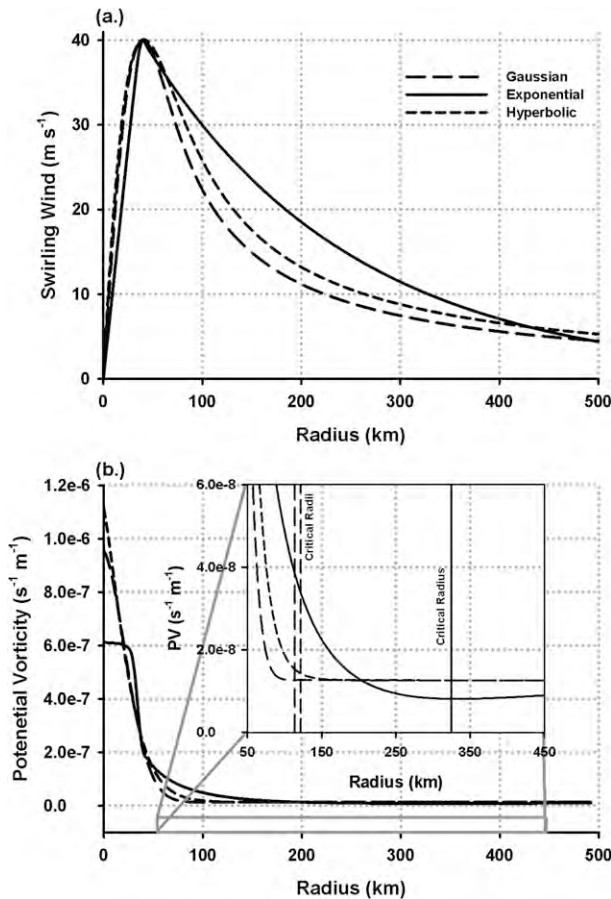


FIG. 2. (a) Initial mean tangential wind and (b) potential vorticity in a 4000-m resting depth layer for the Gaussian, exponential decay ( $X_1 = 208$  km), and hyperbolic vortices. The standard radius of maximum wind is 40 km, and the maximum wind is 40  $\text{m s}^{-1}$ . Critical radii are at 114, 325, and 122 km, and the PV minimum of the exponential vortex is at 338 km (insert).

Rankine, or hyperbolic, vortex of Schecter and Montgomery (2004). Here the smoothness parameter is 2.5, producing a vortex similar to a Gaussian vortex, but with wider PV distribution for the same vortex parameters (Fig. 2b) that produces a PV gradient at the critical radius large enough to suppress the inertia-gravity radiation instability. However, the initial tilt still needs to be small enough to avoid nonlinear inertia-gravity wave radiation instability (Schecter and Montgomery 2006). Our default tilt is 4 km north and 4 km east.

Vortex tracking was tested for accuracy in an idealized experiment. The exponential vortex ( $X_1 = 160$  km) with  $V_{\max} = 30 \text{ m s}^{-1}$ ,  $R_{\max} = 40$  km, linear barotropic initial structure on an  $f$  plane, 500-m layer depths, and  $\sigma_{12} = 0.33$  was initialized with an initial northeast tilt of 14.1 km. The primary damping mechanism through the quasi mode approached equilibrium by 150 days. In no simulation does the vortex ever align perfectly, even

after very long times. The precise center tracking possible with the VTSS formulation allows us to analyze subtle aspects of tilt evolution even at very small amplitude. Moreover, the axially symmetric vortex changes only in response to wave-induced momentum fluxes or secondary flows. The absence of large changes due to friction or heating reveals subtle effects that would be obscured in conventional, full-physics models.

### 3. Alignment in a quiescent environment

#### a. Nonlinear $f$ and $\beta$ plane

##### 1) STANDARD EXPONENTIAL VORTEX

Here we describe 240-h simulations of the exponential-profile vortex tilted initially 5.66 km toward the northeast on  $f$  and  $\beta$  planes. The results include tracks of the upper and lower vortices with respect to the ground, tracks of the upper vortex with respect to the lower one, and time series of separation, or tilt, between the upper and lower vortices. On an  $f$  plane, the upper and lower vortices experience some oscillations, rotate around each other, and converge gradually (Fig. 3). On a  $\beta$  plane, the ground-relative tracks accelerate poleward and westward together (Fig. 4a), as in one-layer simulations (e.g., Willoughby and Jones 2001). The relative track, however, shows converging spirals for the first 48 h, then diverging spirals (Fig. 4b).

During the first 3 h of both simulations, the vortices accelerate toward each other and experience rapidly damped inertia oscillations. Then they begin cyclonic precession around each other because the tilts project onto slowly damped, low-frequency VRWs. High-frequency ( $\sim 3$ -h period) VRWs decay by 18 h because their critical radius is near 62 km, where the mean-vortex PV gradient is stable (Fig. 5a). Their presence depends on the magnitude of the initial tilt. They are usually absent for small tilts ( $\sim 1$  km). Low-frequency VRW energy is partitioned between the sheared VRWs subject to spiral windup and the quasi mode. Their precession period is  $\sim 56$  h. They experience slower damping because their initial critical radius is at 325 km with an initial PV minimum at 338 km. On both  $f$  and  $\beta$  planes, most of the tilt decay from 0 to 12 h stems from VRW shearing. After 12 h, the tilt decreases through exponential decay of the quasi mode, consistent with Reasor et al. (2004).

On an  $f$  plane, the quasi mode converges after 5 days to a  $\sim 120$  m diameter loop. Domain-scale anticyclonic inertia oscillations, with periods  $\sim 33$  h, interfere with the quasi mode to produce a 22-h beat period (Fig. 6) and triangular-shaped relative track orbits after 72 h (Fig. 3b).

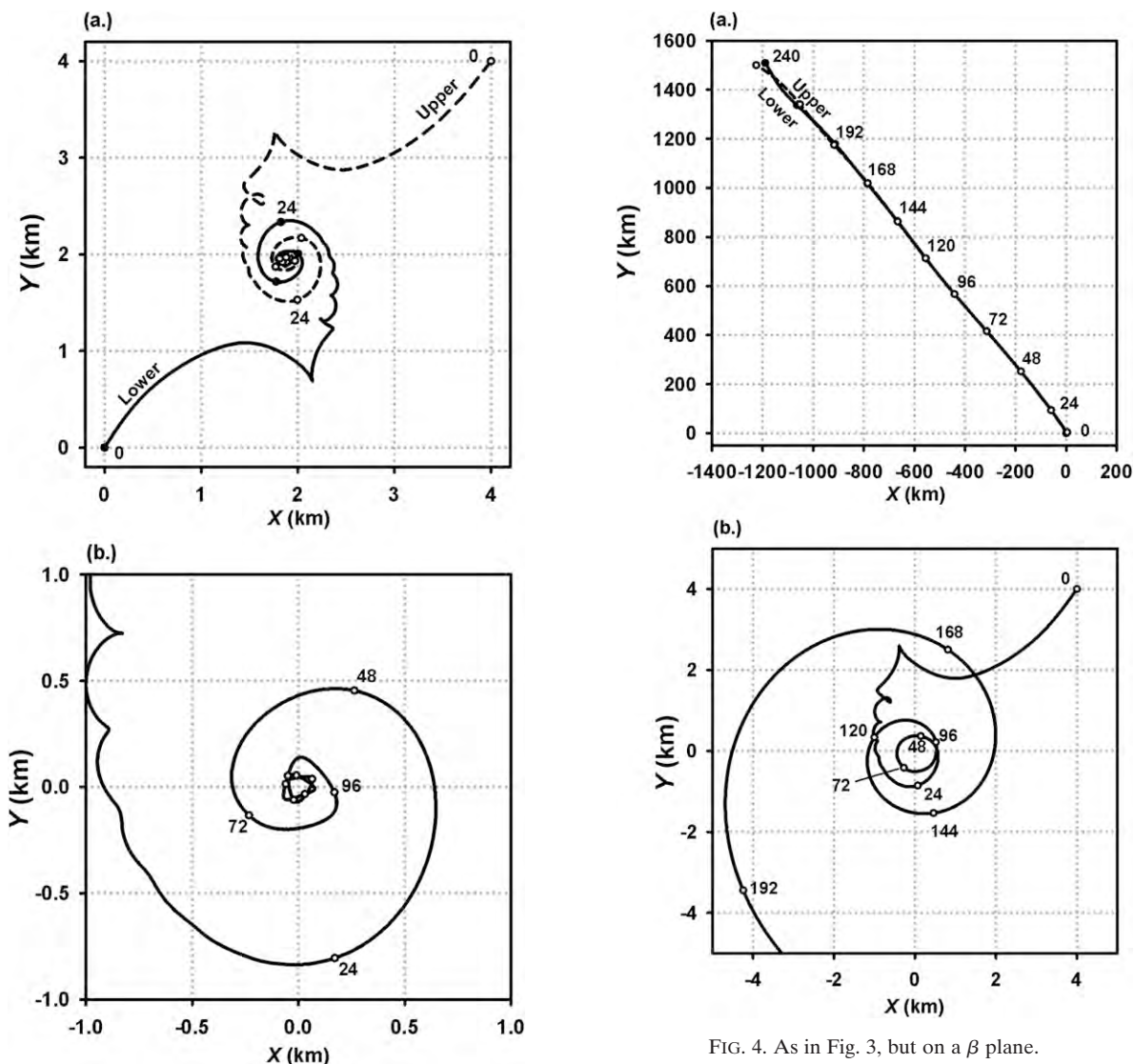


FIG. 3. (a) Tracks for 0–240 h of the lower (solid: closed circles indicating positions at 24-h intervals) and upper (dashed, open circles) vortices initialized on an  $f$  plane and with a 5.66-km initial tilt using the standard exponential decay vortex ( $X_1 = 208$  km). (b) Track of the upper vortex relative to the lower.

By contrast, instability on a  $\beta$  plane arises as the lower-level critical radius and axially symmetric PV minimum both move inward, the latter overtakes the former (Fig. 5a), and the quasi mode precesses at a nearly constant rate (Fig. 6). The  $\beta$  torque weakens the outer axially symmetric wind (Fig. 7a). Simultaneously, eddy momentum transports due to outward propagating, sheared VRWs move the PV minimum inward (Fig. 7b). By 72 h, the critical radius crosses the PV minimum and subsequently remains on its stable side, even as the inflectional instability strengthens. By 192 h, conservation of absolute (potential) vorticity as the

vortex moves poleward establishes a more pronounced PV minimum that supports a large reversed (unstable) PV gradient (Fig. 5b). Beyond the PV minimum, PV increases as a result of increasing  $f$  with a small contribution from the eddy transports by the  $\beta$  gyres (Fig. 7b).

The streamfunction and vorticity are dominated by the  $\beta$  gyres, whose amplitude is an order of magnitude greater than the tilt gyres (Fig. 8). We isolate the tilt gyres by reinitializing the linear  $f$ -plane model with the mean vortex and wavenumber-1 tilt from the nonlinear  $\beta$ -plane solution at 192 h. After transients die away, the VRWs reappear by 240 h (or 48 h after reinitialization). Both the linear tilt and the growth rate for inflectional instability nearly match the nonlinear experiment at 192 h, demonstrating that the instability is essentially linear.

The PV field exhibits two dipoles on opposite sides of the mean-flow PV minimum at  $\sim 325$  km (Fig. 9). The



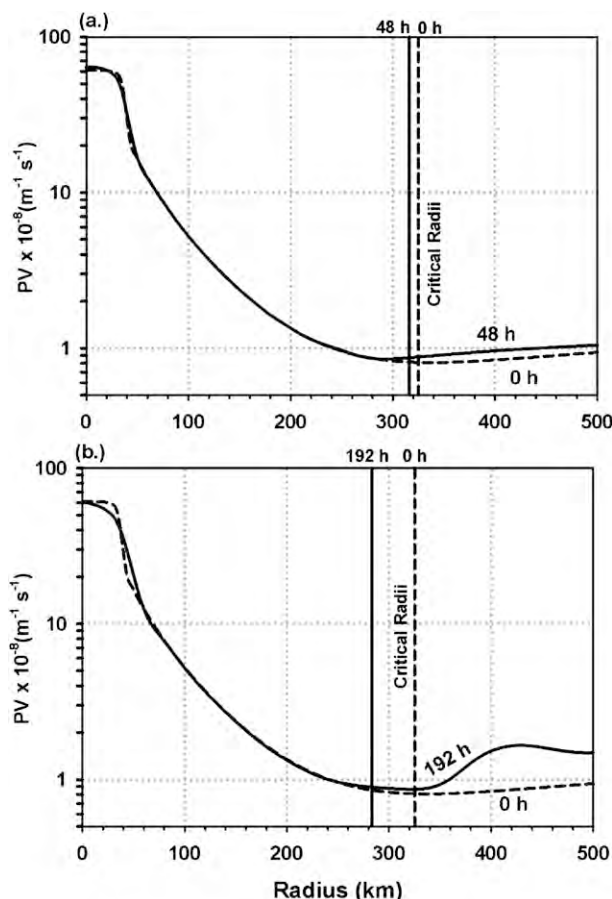


FIG. 5. (a) Mean-vortex PV (solid) in the lower level at 48 h for the standard vortex ( $X_1 = 208$  km) on a  $\beta$  plane. The critical radius is at 316 km with the PV minimum at 292 km. The initial PV (dashed) has a critical radius at 325 km and PV minimum at 338 km. (b) The same initial PV and the PV after 192 h when the critical radius was at 283 km.

relative phase between these features shifts by about  $120^\circ$  across the mean PV minimum and remains locked over time. The essence of the barotropic instability is that phase-shifted VRWs resonate across a PV extremum so that each induces advective PV transports that amplify the other. Thus, each of the counterpropagating (relative to the mean flow) wave trains that rides the reversed gradient causes the other to grow. The term “inflectional instability” emphasizes the essential role of inflection points of the mean PV distribution in maintaining the phase shift over time. Note that Kossin et al. (2000) did not consider wavenumber 1, which is always stable in a barotropic nondivergent model. Still, if one extrapolates its place on their Fig. A1, it is plausibly unstable in the present two-layer shallow-water divergent formulation.

Enhancement of the unstable PV gradient seems to occur in bursts, when the greater vorticity derivative maximum in Fig. 7b splits to straddle the outer vortex

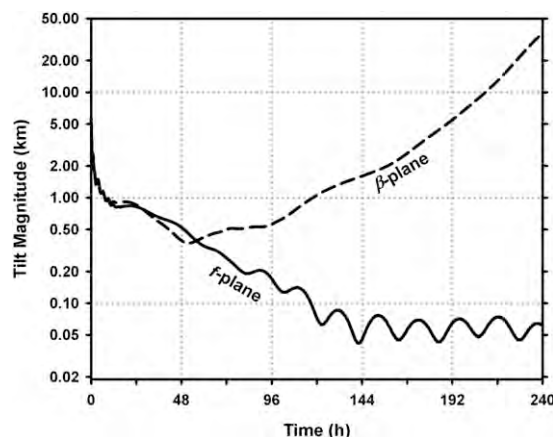


FIG. 6. Separation between of the upper vortex relative to the lower (tilt) as a function of time for nonlinear  $f$  planes (solid) and  $\beta$  planes (dotted) for the standard vortex.

PV maximum. Each time a splitting event occurs, it enhances the unstable PV gradient and causes it to propagate inward, further strengthening the instability by decreasing the separation between the sharp gradients (e.g., Kossin et al. 2000). By 240 h, however, sheared VRWs excited by the growing tilt push the inflection point outward to 410 km and several local PV minima form within the broader minimum. Widening the broad minimum and formation of multiple local PV minima within it seems to be the mechanism for eventual suppression of the inflectional instability.

With baroclinic stratification, tilted vortices always have a small mean tilt so that the quasi mode oscillation period is clear in tilt diagrams. Inertia oscillation interference obscures it on the  $f$  plane in Fig. 6. On a  $\beta$  plane, however, the  $\beta$ -gyre shear strengthens the mean tilt. In the linear model, this shear is always toward the northwest and leads to a superposition of both the southwestward tilt precession and the quasi-mode rotation. In the nonlinear model, the  $\beta$ -gyre shear is initially toward the northwest, but it rotates with the quasi mode or with the track oscillation forced by the time evolution of the  $\beta$  gyres themselves (see below). Although this effect is initially secondary to quasi-mode precession, it becomes dominant as the quasi mode decays.

Inflectional instability extracts energy from the mean flow. Thus, by 240 h, the maximum winds are  $35.6$  and  $31.2$   $m s^{-1}$  in the lower and upper layers, respectively, while  $R_{max}$  propagates outward to 60-km radius. Weakening is always greater in the upper layer.

## 2) STRONG EXPONENTIAL VORTEX

Here we repeat the  $f$ - and  $\beta$ -plane experiments for  $V_{max} = 80$   $m s^{-1}$ ,  $X_1 = 160$  km, and other parameters unchanged (Fig. 10). As before, inertia-gravity oscillations

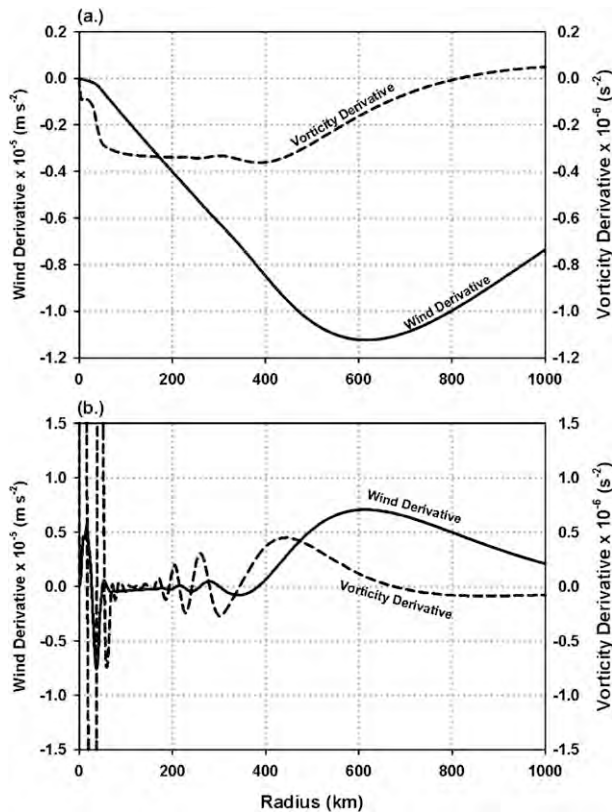


FIG. 7. Radial profiles for the standard vortex at 48 h of tendencies of (a) mean tangential wind (solid) and vorticity (dashed) due to the  $\beta$  torque acting on the symmetric wind in the lower level and (b) the mean tangential wind (solid) and vorticity (dashed) tendencies due to eddy transports.

from the unbalanced initial state damp during the first 6 h, whereas high frequency VRWs decay by 12 h. VRW shearing accounts for most of the damping before 24 h, and quasi-mode decay dominates through 120 h on both the  $f$  and  $\beta$  planes. Inflectional instability dominates after 120 h on the  $\beta$  plane, and inertia oscillations (33-h period) dominate on the  $f$  plane. The initial PV minimum is near a 259-km radius. Tilt precession periods are about 21 h on the  $f$  plane and about 24 h on the  $\beta$  plane. The  $f$ -plane critical radius is at 254 km through 120 h, consistent with quasi-mode damping.

On a  $\beta$  plane, the  $\beta$  torque moves the critical radii inward at both levels from 262 km at 24 h to 242 km at 240 h (Fig. 11). By 24 h, eddy transports due to outward propagating, sheared VRWs move the dominant PV minimum in the lower layer outward to 270 km and the PV minimum in the upper layer inward to 241 km.

The vortex PV profile for the lower level at 192 h of the  $\beta$ -plane experiment has a critical radius of 247 km on the stable side of the PV minimum at 270 km. The steepening of the PV gradient near 360 km occurs a

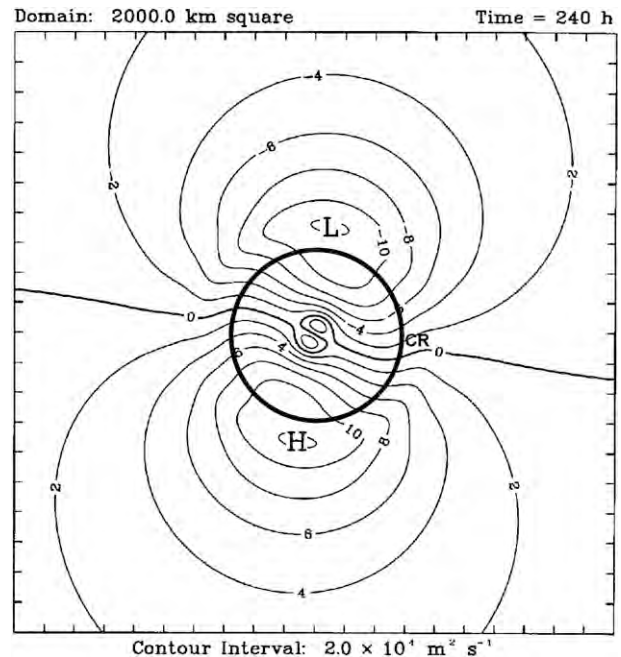


FIG. 8. Wavenumber-1 streamfunction in the lower level after 240 h for the linear continuation on an  $f$  plane of the  $\beta$ -plane run from 192 h in Fig. 5b. The critical radius is 283 km and the contour interval is  $2 \times 10^4 \text{ m}^2 \text{ s}^{-1}$ .

little sooner than in the  $40 \text{ m s}^{-1}$  experiment. Thus, inflectional instability begins when the unstable PV gradients are strong and close to the inner core of the vortex. By 240 h,  $V_{\text{max}}$  in the lower and upper layers has decreased to  $75.4$  and  $75.3 \text{ m s}^{-1}$  at  $R_{\text{max}} = 44 \text{ km}$ . The final tilt is about  $0.6 \text{ km}$ .

#### b. Parameter sensitivity

The principal model parameters are the Coriolis parameter, layer depth, static stability, maximum wind  $R_{\text{max}}$  and, for the exponential vortex,  $X_1$ . Experiments with  $V_{\text{max}} = 10$  to  $80 \text{ m s}^{-1}$  explore the sensitivity of the nonlinear inflectional instability to intensity. The experiments use both the exponential-profile vortex and the hyperbolic or Gaussian-like vortex;  $R_{\text{max}} = 40 \text{ km}$ , and  $X_1 = 240 \text{ km}$  for the exponential-vortex experiments. These parameters correspond to the prehurricane case of Mallen et al. (2005) but also represent hurricanes reasonably well. Reasor et al. (2004) found that increasing Rossby number (which is proportional to  $V_{\text{max}}$ ) causes faster resonant damping on an  $f$  plane. Numerical experimentation shows that this pattern also holds for the exponential vortex.

##### 1) MAXIMUM WIND, STANDARD VORTEX

Table 1 shows the initial critical radii and the tilt precession periods for the standard vortex on an  $f$  plane.

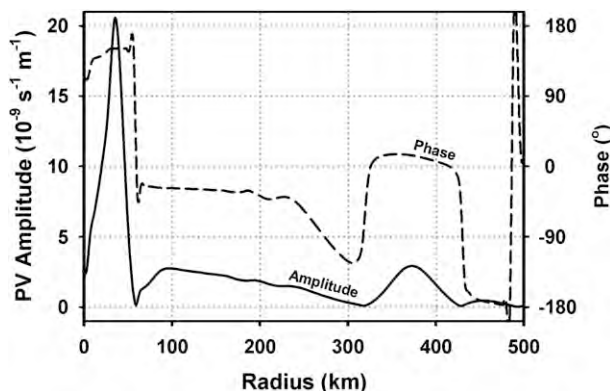


FIG. 9. Wavenumber-1 perturbation PV amplitude and phase after 240 h for a  $40 \text{ m s}^{-1}$  vortex on an  $f$  plane.

The PV minimum remains in essentially the same place over the range of vortex strengths. The PV gradients near the critical radius become sharper as vortex strength increases. In situations when the critical radius changes slowly with time, this pattern causes decreased inflectional instability for stronger  $V_{\max}$ .

Figure 12 summarizes the evolution of vortex tilt as a function of  $V_{\max}$  on  $f$  and  $\beta$  planes. On an  $f$  plane, only the  $10 \text{ m s}^{-1}$  vortex is weakly unstable. Its critical radius lies beyond the symmetric PV minimum. The  $15 \text{ m s}^{-1}$  vortex is nearly neutral. Stronger vortices damp through VRW shearing before 12 h and subsequently through the quasi mode. VRW shearing becomes faster with increasing vortex strength so that the damping curves separate. Quasi-mode damping is also faster in stronger vortices, as noted above.

On an  $f$  plane, the quasi mode decays sufficiently for the inertia oscillations to be dominant by 198 h, 120 h, and 66 h, respectively, for the 30, 40, and  $80 \text{ m s}^{-1}$  simulations. This transition does not occur in the  $40 \text{ m s}^{-1}$  vortex with  $X_1 = 208 \text{ km}$  but does occur at 132 h in the  $80 \text{ m s}^{-1}$  vortex with  $X_1 = 160 \text{ km}$ . Comparison with the  $f$ -plane damping for the  $40 \text{ m s}^{-1}$  vortex (Figs. 6 and 12a) shows faster decay for larger  $X_1$ —that is, for broader vortices where the wind decreases more slowly for  $r > R_{\max}$ . This pattern also holds for the  $80 \text{ m s}^{-1}$  vortex (Figs. 10 and 12a), although it is evident only during the first 12 h.

On a  $\beta$  plane, all vortices experience inflectional instability with the fastest growth of the tilt after 24 h in the  $17.5 \text{ m s}^{-1}$  simulation (Fig. 12b). The  $10 \text{ m s}^{-1}$  simulation has the slowest initial amplification rate, as indicated by the slopes of the curves, while the  $80 \text{ m s}^{-1}$  simulation has the fastest. Between these extremes, amplification rates are similar. Curves for 50, 60, and  $70 \text{ m s}^{-1}$  simulations (not shown) are more like the  $40 \text{ m s}^{-1}$  simulation than the  $80 \text{ m s}^{-1}$  simulation. In fact,

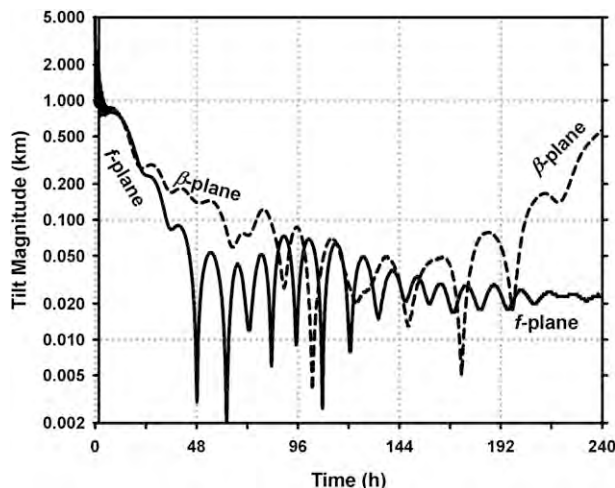


FIG. 10. Position of the upper vortex relative to the lower as functions of time on an  $f$  plane (solid) and  $\beta$  plane (dashed) for the standard vortex:  $X_1 = 160 \text{ km}$ ,  $V_{\max} = 80 \text{ m s}^{-1}$  at 40-km radius.

separation after 240 h for these cases depends on the amount of damping at the beginning of the experiment so that the strongest vortices finish with least tilt.

By 216 h, the inflectional instability of the  $80 \text{ m s}^{-1}$  vortex becomes weak. Its outer PV trough exhibits several extrema that interfere with PV stirring because of alternating weakly stable and unstable gradients (not shown) that apparently arose from VRW shearing during spiral windup of the tilt gyre. This mechanism seems to be a viable one for limiting inflectional instability. Table 1 summarizes  $V_{\max}$  and  $R_{\max}$  after 240 h in  $\beta$ -plane simulations. The upper layers of the most unstable vortices weaken by  $>50\%$ , and the lower layers by  $<20\%$ . Similarly,  $R_{\max}$  in the upper layers becomes much larger than in the lower layers.

## 2) MAXIMUM WIND, HYPERBOLIC VORTEX

Figure 13 shows  $V_{\max}$  sensitivity experiments for hyperbolic vortices, and Table 2 shows critical radii, tilt precession periods, and the approximate radii of the first PV minima. Precession periods are  $1/3$ – $1/8$  of those for the exponential vortex, and the critical radii are much smaller, too. Still, at 24 h PV minima in the lower level could reasonably support inflectional instability.

On an  $f$  plane, the tilts of all vortices damp because the profiles show no initial PV minimum. During the first 24 h, stronger vortices damp faster, as before, but damping is much faster than for equivalent exponential vortices. Figure 3 of Reasor et al. (2004) describes damping of Gaussian vortices with Rossby radii of 628 km on  $f$  planes. Our hyperbolic vortices, with Rossby radius of 900 km and  $R_{\max} = 40 \text{ km}$ , lie on the left side of the abscissa in their diagram. Rossby numbers are 5–40 so

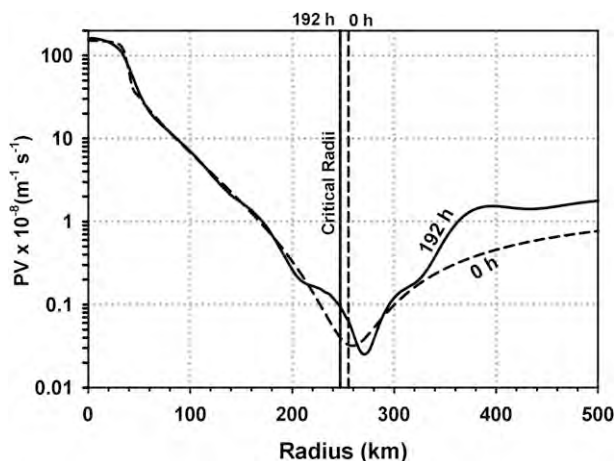


FIG. 11. Mean-vortex PV (solid) after 192 h in the lower level for the  $\beta$ -plane simulation in Fig. 10. The critical radius is at 270 km and the PV minimum at 270 km. The initial PV (dashed) has a critical radius at 262 km and PV minimum at 259 km.

that quasi-mode damping predominates. The  $80 \text{ m s}^{-1}$  vortex lies above the top of the Reasor et al. diagram, but extrapolation of the boundary between the quasi mode and spiral windup regions indicates that the latter mechanism should predominate.

The tilt of the  $80 \text{ m s}^{-1}$  vortex decays much faster than that of any exponential vortex through 12 h (Fig. 13a). The mechanism is initially VRW shearing, then quasi-mode damping. A slowly decaying inertia oscillation dominates the results through the end of the calculation. The critical radius is at 108 km in a strong, stable PV gradient. The other, stronger vortices' tilts are superpositions of decaying quasi modes and inertia oscillations.

On a  $\beta$  plane (Fig. 13b), only the two weakest vortices can become inflectionally unstable when their critical radii lie on the unstable side of the developing PV minimum. Thus, only tropical-depression-strength hyperbolic vortices are subject to nonlinear inflectional instability for the parameters used here.

Nonlinear interactions between the vortex and  $\beta$  force track oscillations (Fig. 14). The  $\beta$  dipole forms by 24 h and intensifies until 48 h when a second dipole forms outside the original one and retards the  $\beta$ -gyre acceleration. The new dipole forms because the Coriolis torque creates anticyclonic flow between 1000 and 3000 km radius. As the original  $\beta$  gyres weaken, the vortex turns a bit more westward (as in Fig. 4) or a lot more westward. The Coriolis torque then starts to weaken the anticyclone and the original  $\beta$  gyres recover, resulting in renewed poleward acceleration by 120 h. Subsequently, a second outer dipole cycle begins. Timing and magnitude differ for different model parameters, but these oscillations are always present.

TABLE 1. Initial  $V_{\max}$ , tilt precession periods, and critical radii for the standard vortex initially with  $X_1 = 240 \text{ km}$ ,  $V_{\max} = 40 \text{ km}$ , and tilt =  $5.7 \text{ km}$  toward the northeast on an  $f$  plane; and  $V_{\max}$  and  $R_{\max}$  after 240 h in the lower (L1) and upper (L2) levels for the same vortex on a  $\beta$  plane. The initial PV minimum was at 389-km radius.

	Initial $V_{\max}$ ( $\text{m s}^{-1}$ )					
	15 ( $f$ )					
	10	17.5 ( $\beta$ )	20	30	40	80
$f$ plane						
Precession period (h)	360	155	132	93	68	34
Critical radius (km)	423	377	375	382	379	379
$\beta$ plane						
240 h $V_{\max}$ ( $\text{m s}^{-1}$ ), L1	8.5	14.2	16.1	26.7	36.4	75.8
L2	7.2	6.6	8.0	24.4	35.5	71.4
240 h $R_{\max}$ (km) L1	60	60	56	52	48	52
L2	80	144	132	64	52	56

Mean tilt from  $\beta$  gyre shear enhances the quasi-mode oscillations (Fig. 13b). As the quasi mode decays in the three strongest vortices, it transforms into an advective track oscillation, with an inertia oscillation superposed in the  $80 \text{ m s}^{-1}$  case. Table 2 summarizes the  $V_{\max}$  and  $R_{\max}$  for each vortex after 240 h. In the  $10 \text{ m s}^{-1}$  vortex, upper-level  $V_{\max}$  decreases by 50%. The four strongest vortices weaken only a little, mostly through horizontal mixing, and their radii of maximum wind remain aligned with little outward migration.

### 3) LATITUDE, EXPONENTIAL VORTEX

We test sensitivity to  $f$  at  $10^\circ$  and  $45^\circ$  latitude on a  $\beta$  plane using both exponential ( $X_1 = 240 \text{ km}$ ) and hyperbolic vortices with  $V_{\max} = 10, 20, 40$ , and  $80 \text{ m s}^{-1}$ . Generally, higher latitude implies faster damping by stable mixing near the critical radius. This effect stems from wider mean-flow PV distributions in higher latitudes because sharper depth gradients are required to balance the same wind with larger  $f$ . Tilt precession is usually faster in higher latitudes and critical radii are smaller, implying stronger resonant damping (Fig. 15).

At  $10^\circ$ , inflectional instability is present in all vortices (Fig. 15a) with fastest vortex tilt growth for  $V_{\max} = 20 \text{ m s}^{-1}$ . The  $V_{\max} = 20$  and  $40 \text{ m s}^{-1}$  simulations terminated at 192 h because an anticyclone formed near the origin, causing the tracking algorithm to fail. The  $80 \text{ m s}^{-1}$  simulation terminated because the instability had run its course. VRW shearing causes most of the damping before 12 h, and the quasi modes are visible in the 40 and  $80 \text{ m s}^{-1}$  simulations. At  $45^\circ$ , the hurricane vortices do not exhibit inflectional instability (Fig. 15b). Weaker vortices become unstable after 144 h. Decay through VRW shearing dominates the first 12 h. Quasi modes appear prominently in the 10 and  $20 \text{ m s}^{-1}$  simulations but are weak in



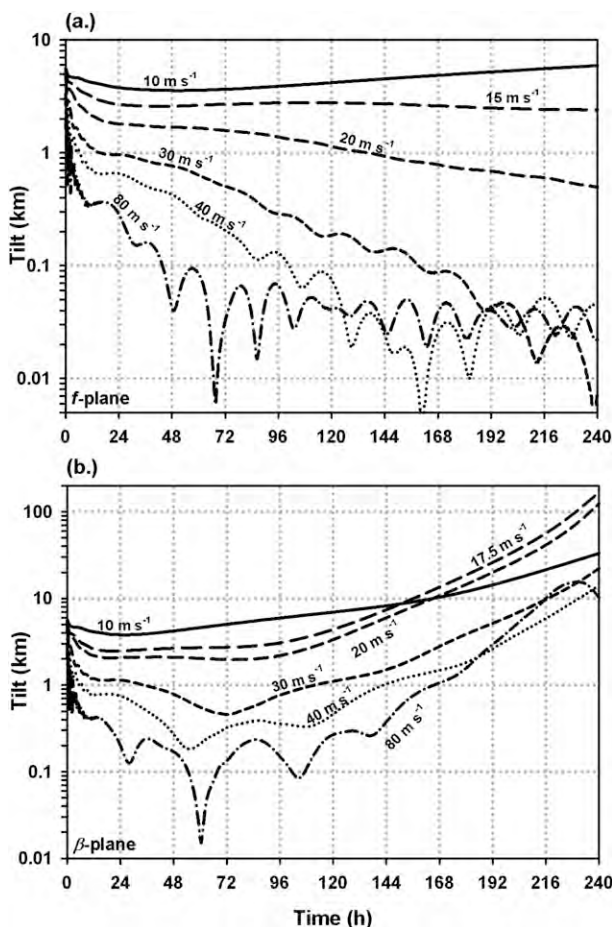


FIG. 12. Position of the upper vortex relative to the lower as a function of time: (a) on an  $f$  plane and (b) on a  $\beta$  plane, for the standard vortex,  $X_1 = 240$  km, vortex with  $R_{\max} = 40$  km, and  $V_{\max} = 10, 15, 20, 30, 40$ , and  $80 \text{ m s}^{-1}$ .

the 40 and  $80 \text{ m s}^{-1}$  simulations, having decayed by 48 and 12 h, respectively. After these times, the  $\beta$ -gyre track oscillations and domain-scale inertia oscillations (period 17 h) dominate. The  $\beta$ -gyre oscillations have 120–144-h periods. All of these vortices maintain their strength and remain nearly barotropic.

#### 4) LATITUDE, HYPERBOLIC VORTEX

The tilt time series for the hyperbolic vortex on the  $\beta$  plane at  $10^\circ$  and  $45^\circ$  appear in Fig. 16. Larger  $f$  generally implies faster initial damping, except in the  $10 \text{ m s}^{-1}$  simulation where the tilt remains nearly constant during the first 36 h. These vortices have  $Ro = 10, 5$ , and  $2.5$ , which lies on approximately the same damping curve in Fig. 3 of Reasor et al. (2004). Stronger vortices lie higher on their diagram and damp more quickly in higher latitudes.

At  $10^\circ$ , only the  $V_{\max} = 10$  and  $20 \text{ m s}^{-1}$  simulations experience inflectional instability, starting at 24 h and

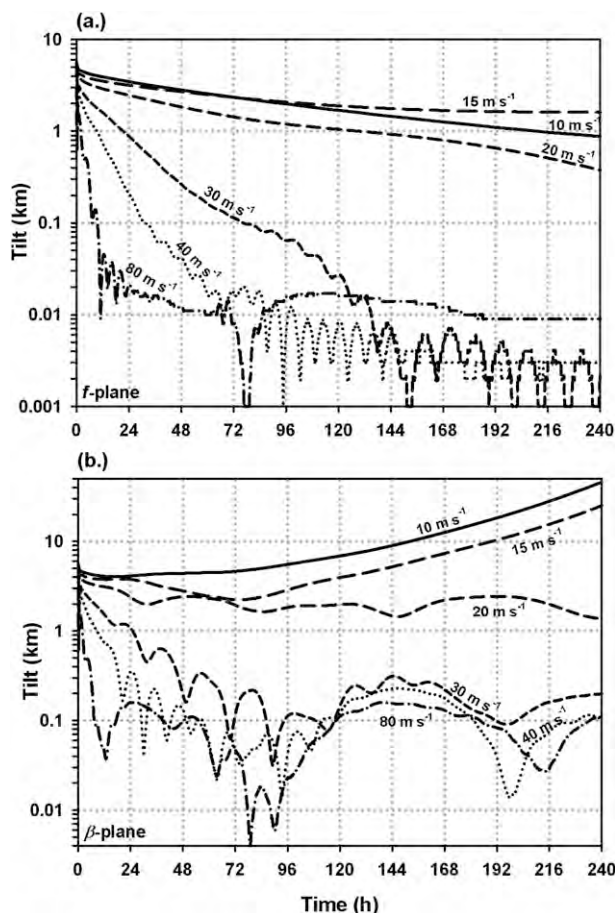


FIG. 13. As in Fig. 12, but for the hyperbolic vortex.

144 h, respectively. The quasi mode is present throughout the  $40 \text{ m s}^{-1}$  simulation, but damps so that the long period  $\beta$ -track oscillation dominates after 96 h. In the  $80 \text{ m s}^{-1}$  simulation, sheared VRWs decay by 12 h and the quasi mode decays by 30 h. Then the long period  $\beta$ -track oscillation takes over, with some inertial oscillations present until  $\sim 96$  h. At  $45^\circ$ , only the  $10 \text{ m s}^{-1}$  vortex becomes inflectionally unstable. Quasi modes dominate the 10 and  $20 \text{ m s}^{-1}$  simulations. In the 40 and  $80 \text{ m s}^{-1}$  simulations, the quasi modes decay by 30 h and 12 h, respectively. Subsequently, long period  $\beta$ -gyre track oscillations with superposed inertial oscillations dominate. When  $\beta$  is smaller, these nonlinear oscillations have longer periods and are so strong that the 40 and  $80 \text{ m s}^{-1}$  vortices turn southward near the middle of the simulations.

#### 5) STATIC STABILITY, DEPTH, AND $R_{\max}$

Larger Rossby radii caused less resonant damping in Fig. 3 of Reasor et al. (2004). Thus, either increased static stability or deeper layers weaken resonant damping through mixing near a critical radius. Numerical



TABLE 2. Initial  $V_{\max}$ , tilt precession period, and critical radii for the hyperbolic vortex on an  $f$  plane; radius of PV minimum after 24 h; and  $V_{\max}$  and  $R_{\max}$  after 240 h in the lower (L1) and upper (L2) levels for the same vortex on a  $\beta$  plane. Initially,  $R_{\max} = 40$  km and tilt = 5.7 km toward the northeast.

	Initial $V_{\max}$ ( $\text{m s}^{-1}$ )					
	10	15	20	30	40	80
<i>f</i> plane						
Precession period (h)	160	62	36	16	10	5
Critical radius (km)	240	184	164	134	122	121
$\beta$ plane						
24-h PV minimum radius (km)	220	250	270	172	180	180
240-h $V_{\max}$ ( $\text{m s}^{-1}$ ), L1	8.8	13.5	18.7	28.6	38.6	78.9
L2	5.3	10.7	18.6	28.6	38.6	78.8
240-h $R_{\max}$ (km) L1	52	48	48	44	44	40
L2	84	64	48	44	44	40

experiments over a wide parameter range confirm this pattern. In these runs, the tilt precession decreases, moving the critical radius outward to unstable (or less stable) PV gradients. The PV minimum location is insensitive to static stability or layer depth.

Schecter and Montgomery (2007) showed that latent heating reduces effective static stability, leading to faster tilt precession that may suppress unstable inertia-gravity wave radiation. This effect should work with inflectional instability as well. The hyperbolic vortex sensitivity to  $R_{\max}$  and  $f$  is similar because  $R_{\max}$  enters Fig. 3 of Reasor et al. (2004) as a product with  $f$ . Generally, larger  $R_{\max}$  leads to faster damping for stronger vortices, but for the exponential vortex, larger  $R_{\max}$  generally causes slower damping because both  $X_1$  and  $R_{\max}$  control the PV distribution. In the Gaussian vortex  $R_{\max}$  by itself controls the width of the PV distribution. For the exponential decay vortex, as noted above, increasing  $X_1$  increases damping through mixing near the critical radius by moving the critical radius inward to a more stable PV gradient.

#### 4. Summary

The responses of a two-layer, nonlinear, semispectral model of hurricane-like vortices to an initially imposed tilt provide insight into vortex recovery from environmental shear. Model spectral representation is truncated at wavenumber 3, but most results were verified with wavenumber 6 (not shown). Realistic static stability requires a slightly baroclinic mass distribution.

Tilted vortices have a brief initial period of unbalanced converging acceleration. Continued damping depends upon the partition of energy between sheared VRWs of the spiral-windup solution and the quasi

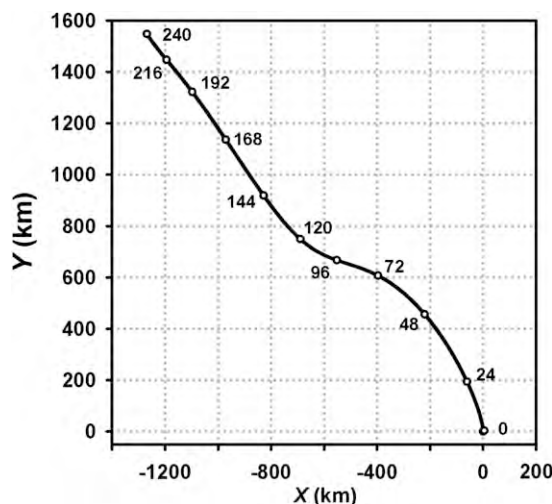


FIG. 14. Track for the lower vortex with an initial tilt = 5.66 km toward the northwest on a  $\beta$  plane using the standard hyperbolic vortex.

mode. Sheared VRWs always damp the tilt, primarily through filamentation of tilt PV in the radially shearing mean flow. This process generally dominates during the first 24 h. The quasi mode often decays by resonance with the mean flow at a critical radius where the axially symmetric PV gradient is negative. When the PV gradient is positive, inflectional (barotropic or baroclinic) instability occurs.

A new result here is creation of inflectional instability on a  $\beta$  plane by wave-mean flow interactions. Cyclonic vortices form  $\beta$  gyres as the axially symmetric winds advect the planetary PV gradient. The resulting stream-function dipole supports a current across the vortex, leading to westward and poleward vortex propagation with near-conservation of mean-flow PV in the inner part of the vortex. The  $\beta$  gyres also interact with the planetary PV gradient to spin up anticyclonic symmetric winds on the vortex periphery. Because PV is very nearly conserved in the inner part of the vortex, an outer PV minimum arises as the vortex moves poleward and encounters larger planetary vorticity. In this way, vortices can destabilize through formation of an outer PV minimum that meets the necessary condition for inflectional instability.

The vortices studied here are Gaussian-like PV monopoles with fast tilt precession and exponential outer-wind-profile vortices with slower precession. For the standard parameters, exponential vortices destabilize through nonlinear inflectional instability on a  $\beta$  plane for all intensities, except at latitude  $>45^\circ$ , where only the weakest vortex destabilizes. For the Gaussian-like vortices, inflectional instability develops only for tropical depression strength, while tropical storm and hurricane strength vortices remain stable.

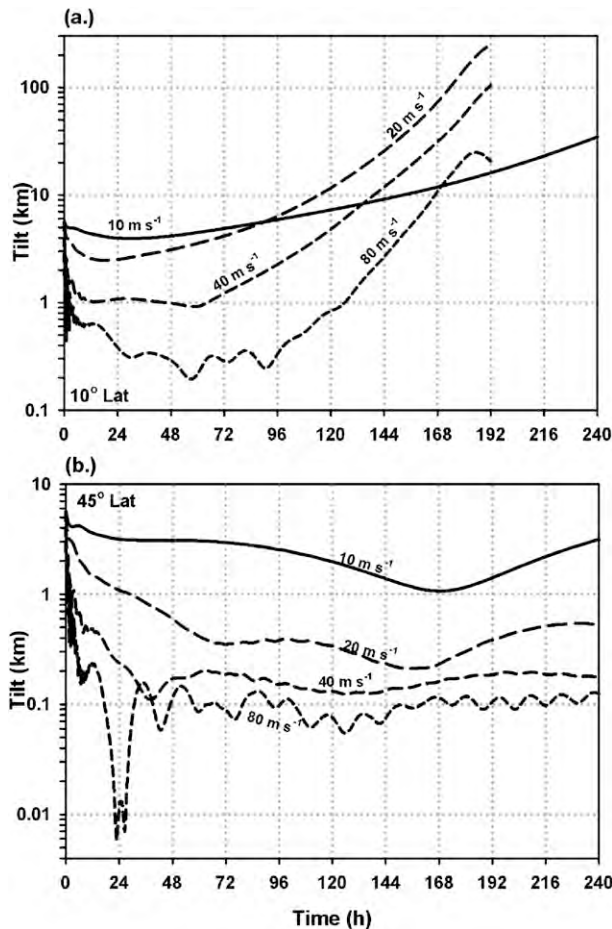


FIG. 15. As in Fig. 12, but for the exponential vortex:  $X_1 = 240$  km at (a) 10° and (b) 45° latitude on a  $\beta$  plane and initial maximum wind speeds 10, 20, 40, and 80 m s<sup>-1</sup>.

The sensitivity of inflectional instability to model parameter changes confirms the Gaussian vortex results of Reasor et al. (2004). Stronger vortices, larger radii of maximum wind, weaker static stability, shallower fluid depth, and higher latitude inhibit inflectional instability. The exponential decay vortex exhibits the same pattern, except that smaller  $R_{\max}$  causes less inflectional instability, as does larger  $X_1$ . In Gaussian-like vortices,  $R_{\max}$  controls the PV distribution width, whereas in exponential vortices both  $R_{\max}$  and  $X_1$  control the PV distribution width. The combined roles of these two parameters account for the different sensitivity of these vortices to changes in  $R_{\max}$ .

When inflectional instability is present, the mean vortex weakens as amplifying VRWs draw energy from the mean flow. The radius of maximum wind also expands. The greatest changes are in the upper layer so that in some cases the radii of maximum wind no longer overlap. For strong instability, the upper vortex some-

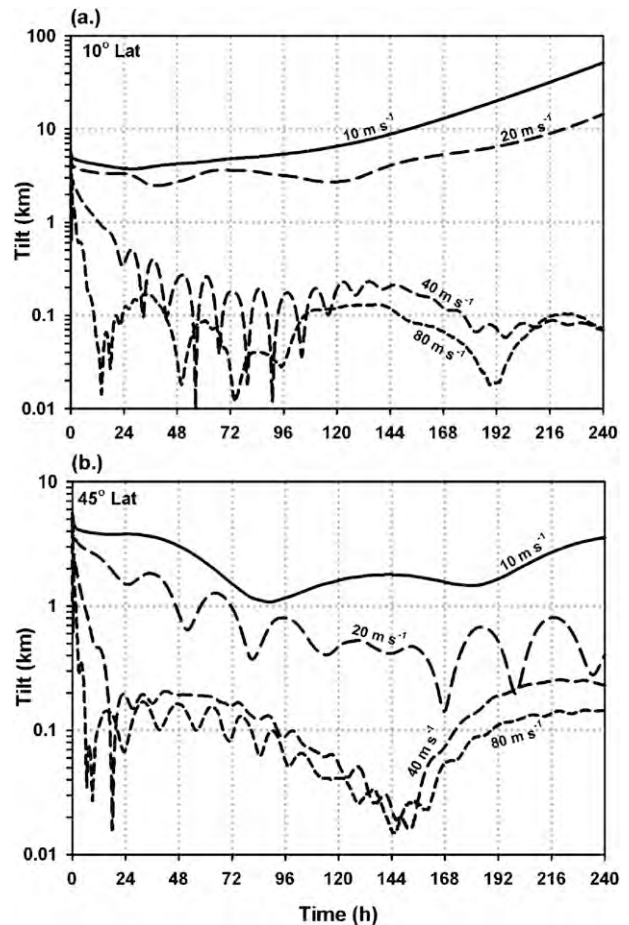


FIG. 16. As in Fig. 15, but for the hyperbolic vortex at (a) 10° and (b) 45° latitude.

times dissipates, while a much weakened lower vortex survives. The nonlinear inflectional instability should mean that atmospheric vortices are less resilient to environmental vertical shear on a  $\beta$  plane than on an  $f$  plane, provided that stabilization of the inflectional instability through reduction in effective static stability as a result of condensation may be neglected.

**Acknowledgments.** The first two authors' efforts were supported through NSF Grant ATM-0454501. We are also grateful to Frank Marks and the staff at NOAA's Hurricane Research Division for administrative and computer support of RWJ's participation.

## REFERENCES

- Black, M. L., J. F. Gamache, F. D. Marks Jr., C. E. Samsury, and H. E. Willoughby, 2002: Eastern Pacific Hurricanes Jimena of 1991 and Olivia of 1994: The effect of vertical shear on structure and intensity. *Mon. Wea. Rev.*, **130**, 2291–2312.

- Frank, W. M., and E. A. Ritchie, 1999: Effects of environmental flow upon tropical cyclone structure. *Mon. Wea. Rev.*, **127**, 2044–2061.
- , and —, 2001: Effects of vertical wind shear on the intensity and structure of numerically simulated hurricanes. *Mon. Wea. Rev.*, **129**, 2249–2269.
- Jones, S. C., 1995: The evolution of vortices in vertical shear. I: Initially barotropic vortices. *Quart. J. Roy. Meteor. Soc.*, **121**, 821–851.
- Kossin, J. P., W. H. Schubert, and M. T. Montgomery, 2000: Unstable interactions between a hurricane's primary eyewall and a secondary ring of enhanced vorticity. *J. Atmos. Sci.*, **57**, 3893–3917.
- Mallen, K. J., M. T. Montgomery, and B. Wang, 2005: Re-examining the near-core radial structure of the tropical cyclone primary circulation: Implications for vortex resiliency. *J. Atmos. Sci.*, **62**, 408–425.
- Möller, J. D., and M. T. Montgomery, 1999: Vortex Rossby waves and hurricane intensification in a barotropic model. *J. Atmos. Sci.*, **56**, 1674–1687.
- Montgomery, M. T., and R. J. Kallenbach, 1997: A theory of vortex Rossby waves and its application to spiral bands and intensity changes in hurricanes. *Quart. J. Roy. Meteor. Soc.*, **123**, 435–465.
- , J. D. Möller, and C. T. Nicklas, 1999: Linear and nonlinear vortex motion in an asymmetric balance shallow water model. *J. Atmos. Sci.*, **56**, 749–768.
- Nolan, D. S., and M. T. Montgomery, 2000: The algebraic growth of wavenumber-1 disturbances in hurricane-like vortices. *J. Atmos. Sci.*, **57**, 3514–3538.
- Ooyama, K. V., 1969: Numerical simulation of the life cycle of tropical cyclones. *J. Atmos. Sci.*, **26**, 3–40.
- Reasor, P. D., M. T. Montgomery, and L. D. Grasso, 2004: A new look at the problem of tropical cyclones in vertical shear flow: Vortex resiliency. *J. Atmos. Sci.*, **61**, 3–22.
- Schecter, D. A., and M. T. Montgomery, 2004: Damping and pumping of a vortex Rossby wave in a monotonic cyclone: Critical layer stirring versus inertia–buoyancy wave emission. *Phys. Fluids*, **16**, 1334–1348.
- , and —, 2006: Conditions that inhibit the spontaneous radiation of spiral inertia–gravity waves from an intense mesoscale cyclone. *J. Atmos. Sci.*, **63**, 435–456.
- , and —, 2007: Waves in a cloudy vortex. *J. Atmos. Sci.*, **64**, 314–337.
- Willoughby, H. E., 1992: Linear motion of a shallow-water barotropic vortex as an initial-value problem. *J. Atmos. Sci.*, **49**, 2015–2031.
- , 1994: Nonlinear motion of a shallow water barotropic vortex. *J. Atmos. Sci.*, **51**, 3722–3744.
- , 1995: Normal-mode initialization of barotropic vortex motion models. *J. Atmos. Sci.*, **52**, 4501–4514.
- , and R. W. Jones, 2001: Nonlinear motion of a barotropic vortex in still air and in an environmental zonal flow. *J. Atmos. Sci.*, **58**, 1907–1923.
- , R. W. R. Darling, and M. E. Rahn, 2006: Parametric representation of the primary hurricane vortex. Part II: A new family of sectionally continuous profiles. *Mon. Wea. Rev.*, **134**, 1102–1120.